Universitat Autònoma de Barcelona

Dipòsit digital de documents de la UAB

This is the **submitted version** of the journal article:

Bigiani, Lorenzo; Hassan, Mariam; Peddis, Davide; [et al.]. «High magnetic coercivity in nanostructured Mn3O4 thin films obtained by chemical vapor deposition». ACS Applied Nano Materials, Vol. 2, issue 3 (March 2019), p. 1704-1712. DOI 10.1021/acsanm.9b00141

This version is available at https://ddd.uab.cat/record/271929

under the terms of the IN COPYRIGHT license

High Low-Temperature Coercivity in Mn_3O_4 Thin Films Obtained by Chemical Vapor Deposition

Lorenzo Bigiani[†], Mariam Hassan[b,c], Davide Peddis[b], Chiara Maccato[a,*], Gaspare Varvaro[b,*], Cinzia Sada[d], Elza Bontempi[e], Sara Martí-Sánchez[f], Jordi Arbiol[f,g], Davide Barreca[h]

[a] *Department of Chemical Sciences, Padova University and INSTM, 35131 Padova, Italy*

[b] *CNR-ISM, Monterotondo Scalo, 00015 Roma, Italy*

[c] *Department of Matter Sciences and Engineering, Environment and Urban Planning, Marche Polytechnic University, 60121 Ancona, Italy*

[d] *Department of Physics and Astronomy, Padova University and INSTM, Padova, Italy*

[e] *Chemistry for Technologies Laboratory, Department of Mechanical and Industrial Engineering, Brescia University and INSTM, Brescia, Italy*

[f] *Catalan Institute of Nanoscience and Nanotechnology (ICN2), CSIC and BIST, Bellaterra, 08193 Barcelona, Catalonia, Spain*

[g] *ICREA, Pg. Lluís Companys 23, 08010 Barcelona, Catalonia, Spain*

[h] *CNR-ICMATE and INSTM, Department of Chemical Sciences, Padova University, 35131 Padova, Italy*

[*] Corresponding authors; phone: +39-0498275234; e-mail: chiara.maccato@unipd.it (C.M.); phone: +39-0690672651; e-mail: gaspare.varvaro@ism.cnr.it (G.V.).

ABSTRACT: High-quality α-Mn_3O_4 (*haussmannite*) thin films consisting of evenly interconnected nanoaggregates were prepared on Si(100) substrates by chemical vapor deposition. The use of different reaction atmospheres (dry *vs*. wet O_2) and total pressures enabled to tailor the system structural and morphological features. The obtained films showed bulk-like magnetic properties together with an extraordinarily high low-temperature in-plane coercivity (up to ≈ 1 T) dependent on the microstructural defect content. These issues may foster the implementation of the obtained films in eventual technological applications.

KEYWORDS: Mn_3O_4, thin films, chemical vapor deposition, magnetic properties, coercivity.

■ INTRODUCTION

Nanostructured magnetic spinel oxides have been widely investigated over the last two decades owing to the possibility of finely tuning their structural, chemical and physical properties by varying the metal cations and their distribution among tetrahedral and octahedral sites.[1-4] Among the family members, α-Mn_3O_4 (*haussmannite*), one of the most stable manganese oxides endowed with large natural abundance, cost-effectiveness and environmental compatibility,[5-7] has been attracting an ever increasing interest. In fact, its chemico-physical properties render it an attractive multi-functional platform for various applications, including, among others, super-/pseudo-capacitors,[8-13] electrodes for batteries,[7,14-15] gas sensors,[16-17] heterogeneous catalysts,[5,10,18] and soft magnetic materials.[19] In particular, bulk Mn_3O_4 is magnetically ordered at 42 K to form a collinear ferrimagnetic array,[20-21] whereas at lower temperatures a canted spin array is produced.[22-24] Since the system magnetic properties are directly dependent on the aggregate size and shape,[2-3,25-27] as well as on their structural features and the presence of defects,[28-30] nanostructured Mn_3O_4 systems in the form of nanoparticles[20,24,30-32] and nanorods/wires[19,21-22,29,33] fabricated by means of different synthesis techniques have been widely studied over the last years. In comparison to these cases, magnetic characteristics of Mn_3O_4 thin films have been scarcely investigated,[20,32] and further efforts in this regard are undoubtedly of importance from both a fundamental and an applicative point of view. Indeed, advances in the fabrication of these systems is a strategic subject of ongoing investigations in order to control the resulting magnetic properties.

In the present work, chemical vapor deposition (CVD), a versatile bottom-up route for the preparation of thin films and nanostructures with specific properties,[6,34] was used to deposit high-quality α-Mn_3O_4 films. In particular, the latter were prepared under both dry O_2 and O_2+H_2O reaction atmospheres and at different pressures (3.0 and 10.0 mbar). The target systems are investigated in their structure, morphology and chemical composition, and their

magnetic properties are characterized as a function of the adopted processing conditions. To the best of our knowledge, there have been no literature reports on the magnetic properties of CVD Mn_3O_4 materials up to date.

■ EXPERIMENTAL SECTION

Material preparation. A cold-wall CVD reactor was used for the synthesis of manganese oxide films, using $Mn(hfa)_2$•TMEDA[35] as Mn precursor (Hhfa = 1,1,1,5,5,5-hexafluoro-2,4-pentanedione; TMEDA = *N*,*N*,*N'*,*N'*-tetramethylethylenediamine; vaporization temperature = 65°C). Precursor vapors were transported by an O_2 flow [purity = 6.0; rate = 100 standard cubic centimeters per minute (sccm)] into the reaction chamber, in which an auxiliary oxygen flow (100 sccm) was also introduced. Growth processes were performed under dry O_2 and O_2+H_2O atmospheres. In the latter case, the auxiliary O_2 flow was passed through a water reservoir maintained at 35°C before entering the reactor. Depositions were carried out for 1 h on pre-cleaned *p*-type Si(100) substrates (MEMC®, Merano, Italy). Basing on preliminary optimizations, the growth temperature was set at 500°C, whereas the total pressure was fixed either at 3.0 or at 10.0 mbar.

Material characterization. Two-dimensional X-ray diffraction (XRD^2) analyses were carried out in reflection mode on a Dymax-RAPID X-ray micro-diffractometer (CuKα radiation), equipped with a cylindrical imaging plate detector, that allows data collection from 0 to 160° (2θ) horizontally and from - 45 to + 45° (2θ) vertically. A collimator diameter of 300 μm and an exposure time of 40 min were used. Conventional XRD patterns were obtained by 2D image integration.

Field emission-scanning electron microscopy (FE-SEM) analyses were performed by means of a Zeiss SUPRA 40 VP instrument, using primary beam voltages between 10 and 20 kV.

The mean thickness and nanoaggregate dimensions were evaluated by the ImageJ software (https://imagej.nih.gov/ij/, accessed December 2018).

High resolution-transmission electron microscopy (HR-TEM) and high angle annular dark field-scanning TEM (HAADF-STEM) analyses were carried out with a FEI Tecnai F20 TEM microscope operated at 200 kV. Sample preparation was performed by means of diamond wire saw cutting, mechanical thinning with diamond lapping films, and ion milling in a Gatan precision ion polishing (PIPS) system. Oxidation state maps were obtained through scanning TEM-electron energy loss spectroscopy (STEM-EELS) analysis by estimating the MnL_3/MnL_2 edge intensity ratio after background subtraction and applying a Gaussian fitting on both edges.[36]

X-ray photoelectron spectroscopy (XPS) measurements were performed on a PerkinElmer Φ 5600ci spectrometer using a standard Al Kα radiation (1486.6 eV). Binding energy (BE) values (uncertainty = ± 0.2 eV) were corrected for charging effects by assigning a BE of 284.8 eV to the adventitious C1s peak.[37-38] Atomic percentages (at. %) were calculated by peak integration, using Φ V5.4A sensitivity factors.

Secondary ion mass spectrometry (SIMS) analysis was carried out by a Cameca IMS 4f instrument, using a Cs^+ primary ion beam (14.5 keV, 20 nA) and negative secondary ion detection, using an electron gun for charge compensation. Rastering over a 150×150 μm^2 area was performed, and secondary ions were collected from a 8×8 μm^2 sub-region to avoid crater effects. Beam blanking mode and high mass resolution configuration were adopted. The sputtering time in the profile abscissa was converted into depth using the mean film thickness values measured by cross-sectional FE-SEM analyses.

Temperature-dependent magnetization measurements were performed by using a superconducting quantum interference device (SQUID) magnetometer (MPMS 10) with the external field applied either in the film-plane or along the surface normal.

■ RESULTS AND DISCUSSION

The system structure, with particular attention to the presence of possible orientation effects, was investigated by the joint use of XRD and XRD^2 experiments. The results shown in Figure 1(a-b) clearly indicated the presence of the tetragonal α-Mn_3O_4 polymorph (Figure 1c; space group $I4_1/amd$; a = 5.762 Å, c = 9.470 Å) with a spinel-type structure.[21,28,39] No other reflections from different Mn oxides were present, indicating the selective formation of phase-pure α-Mn_3O_4, at variance with previous studies.[22-23,29] A closer inspection of Figure 1a revealed an inhomogeneous intensity distribution along the Debye rings, suggesting the occurrence of preferential growth orientation. This effect was particularly evident for the specimen obtained in O_2+H_2O at 3.0 mbar, which was preferentially oriented along the (101) direction, as also revealed by conventional XRD analyses (Figure S1). Indeed, the obtained patterns highlighted the occurrence of different relative peak intensities with respect to the reference *haussmannite*,[39] as well as different intensity ratios between samples grown in dry O_2 and in O_2+H_2O reaction atmospheres. In particular, specimens fabricated in dry O_2, irrespective of the used pressure, presented two main reflections pertaining to (211) and (220) planes, the latter exhibiting a higher relative intensity if compared with the reference pattern. On the other hand, specimens fabricated in O_2+H_2O showed a (211) intensity decrease and a concomitant increase of (101) and (103) signals with respect to the reference powder spectrum. These findings, combined with the texture coefficient (TC) values (§ S-1 and Table 1), suggest an enhanced (220) or (101) orientation and/or a concomitant anisotropic growth for samples obtained in O_2 and in O_2+H_2O atmospheres, respectively. This effect was particularly marked for the system obtained at 3.0 mbar in O_2+H_2O (TC_{101} = 2.3).

XRD data were also used to determine the dislocation density (δ) (Table 1), which resulted

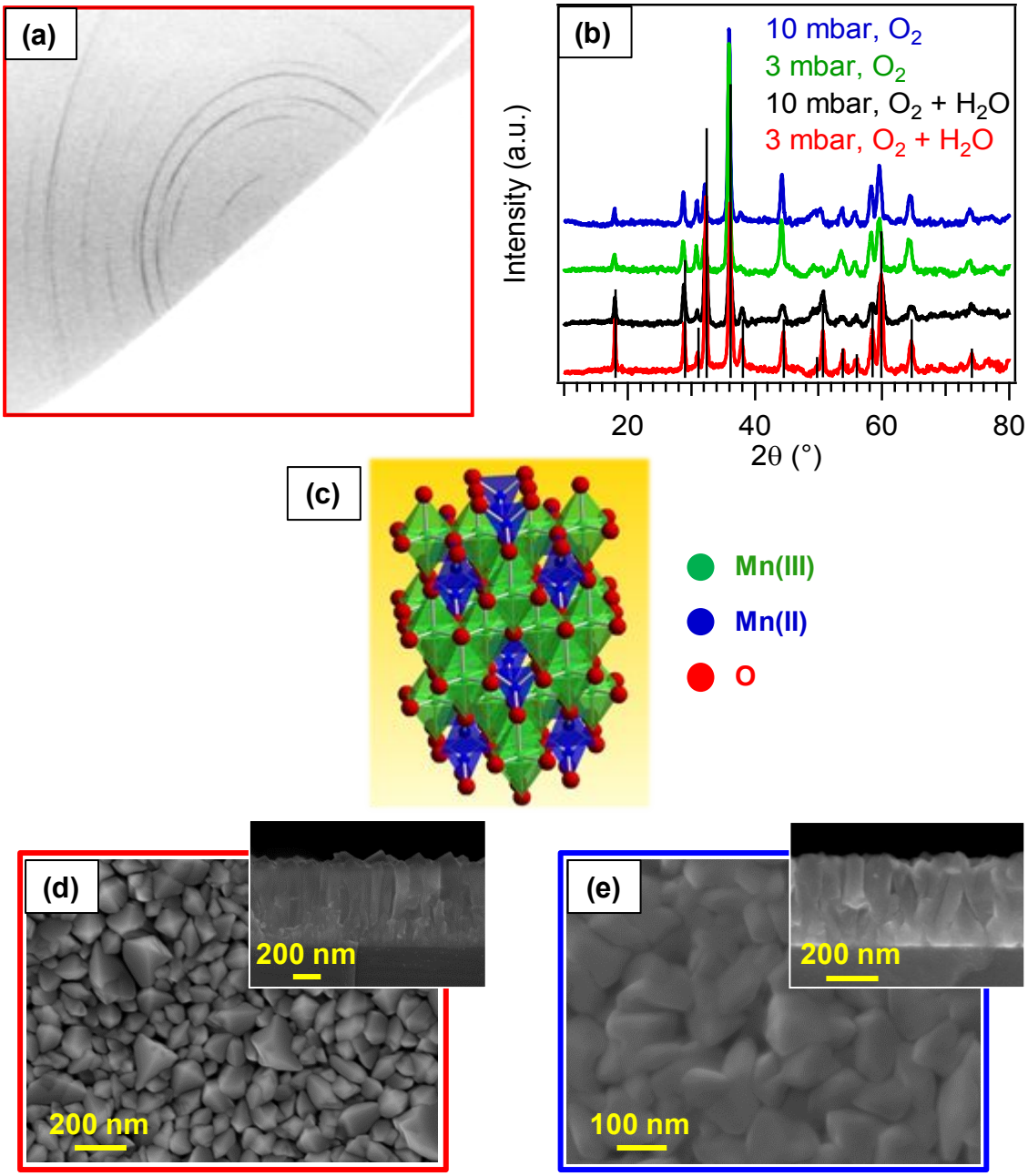

Figure 1. (a) XRD[2] map for a manganese oxide thin film deposited at 3.0 mbar in O_2+H_2O. (b) Integrated XRD patterns for specimens fabricated under different conditions. Vertical black lines mark peak positions for tetragonal α-Mn_3O_4 (*hausmannite*). (c) Representation of the α-Mn_3O_4 crystalline structure [39]. Plane-view FE-SEM micrographs of samples obtained under (d) O_2+H_2O, 3.0 mbar; (e) O_2, 10.0 mbar. The corresponding cross-sectional images are reported as insets.

higher for samples obtained under dry O_2 and, in particular, for the one fabricated at 10.0

mbar (δ = 7.4×10^{14} lines/m^2). These results suggested an increase in the content of microstructural defects under dry O_2 and, in particular, at a pressure of 10.0 mbar.

Sample	TC	δ (lines/m^2)	T (K)	$H_{c,//}$ (T; 5 K)
3 mbar, O_2+H_2O	2.3 (101)	5.6×10^{14}	42±2	0.88
10 mbar, O_2+H_2O	1.5 (101)	5.4×10^{14}	42±2	0.89
3 mbar, O_2	1.5 (220)	7.2×10^{14}	41±2	0.91
10 mbar, O_2	1.5 (220)	7.4×10^{14}	42±2	0.97

Table 1. Texture coefficients (TC) and dislocation density (δ) values, along with phase transition temperatures (T; uncertainty = ± 2 K) and in-plane coercivity ($H_{c,//}$) values for the Mn_3O_4 specimens analyzed in the present work.

A preliminary investigation of material morphology was carried out by means of FE-SEM, which evidenced an optimal film/substrate adhesion. The system nano-organization (Figures 1d,e and S2) was dominated by the occurrence of extensively interconnected nanoaggregates, typical of a three-dimensional growth mode, with a direct influence of the adopted working pressure on film morphology and thickness. In particular, irrespective of the reaction atmosphere, samples obtained at 10.0 mbar presented pseudo-columnar nanostructures (mean diameter = 100 nm; average thickness = 350 nm), whereas, for specimens obtained at 3.0 mbar, imaging revealed the occurrence of more faceted aggregates (mean dimensions = 100 nm; average thickness = 630 nm), similarly to Mn_3O_4 films obtained by pulsed laser deposition.[8]

An additional important insight into Mn_3O_4 nanostructure was gained by TEM analyses on representative samples (Figures 2 and S3). In both cases, Mn_3O_4 formed a polycrystalline layer on the top of the Si(100) substrate with crystalline domains that, in agreement with XRD results, comprised the sole Mn_3O_4 tetragonal phase. The absence of epitaxial relations

between the Si(100) substrate and Mn_3O_4 was due to Si oxidation at the film/substrate interface, resulting in the formation of a thin SiO_2 layer (≈ 2 nm). Further analyses carried out by STEM-EELS enabled to perform a chemical map of manganese valence state by examining the intensity ratios between Mn L_3 and L_2 edges.[36] The results highlighted the even coexistence of Mn(II) and Mn(III) oxidation states (Figures 2d,e), in agreement with the above compositional results, as also confirmed by XPS data (see below).

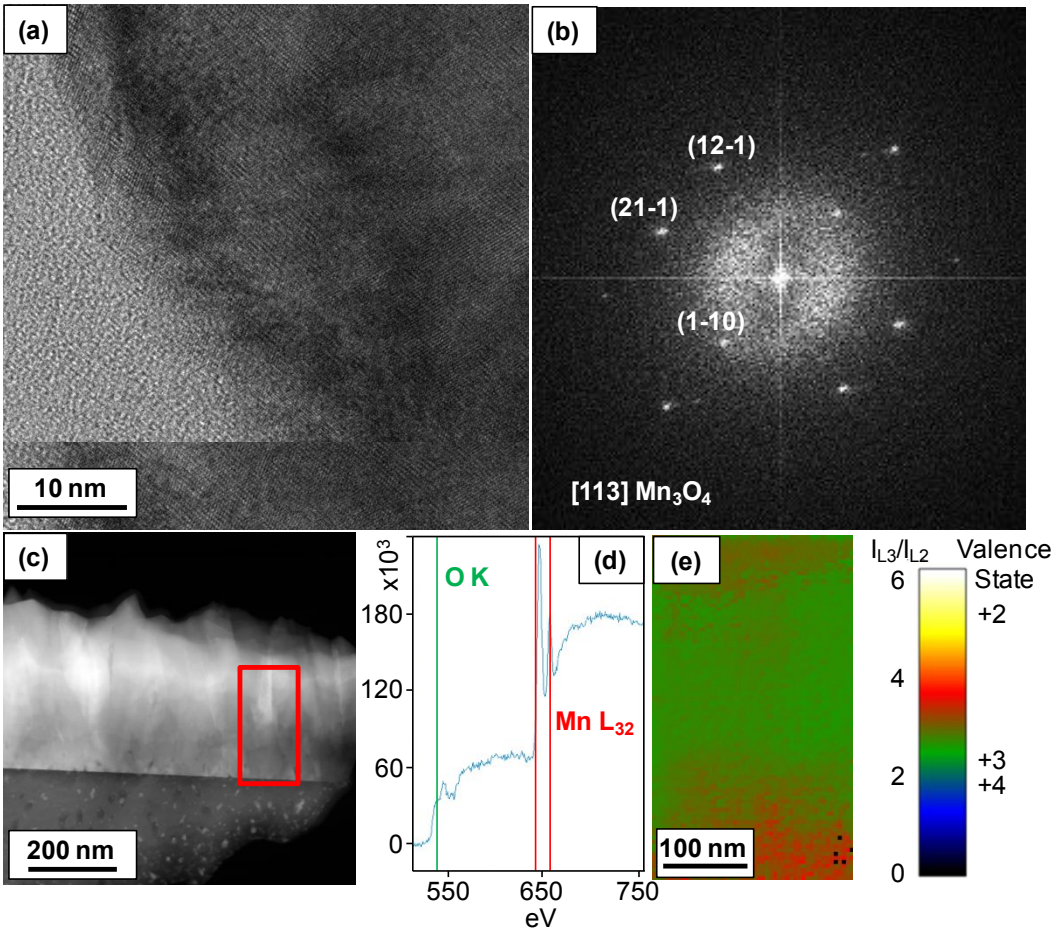

Figure 2. TEM analyses on a Mn_3O_4 thin film deposited at 10.0 mbar under dry O_2. (a) HR-TEM micrograph and (b) corresponding power spectrum. (c) Low magnification cross-sectional HAADF-STEM image. (d) O and Mn EELS signals recorded on the region marked by a red rectangle in (c). (e) Oxidation state map obtained by the MnL_3/MnL_2 edge intensity ratio (I_{L3}/I_{L2}).

The system surface and in-depth chemical composition were investigated by combining XPS

and SIMS analyses. Wide scan XPS spectra (Figure 3a) evidenced the presence of manganese and oxygen, along with adventitious surface carbon contamination. The $Mn2p_{3/2}$ signal position [binding energy (BE) = 641.9 eV] and the corresponding spin–orbit splitting value (11.5 eV; Figure 3b) indicated the formation of pure Mn_3O_4,[5,9,14-15,21,28,38] as also confirmed by the Mn3s multiplet splitting separation (Δ = 5.4 eV, Figure 3c),[6,11,16-17,34] which yielded a finger- print for the sole presence of this oxide, in agreement with structural results.

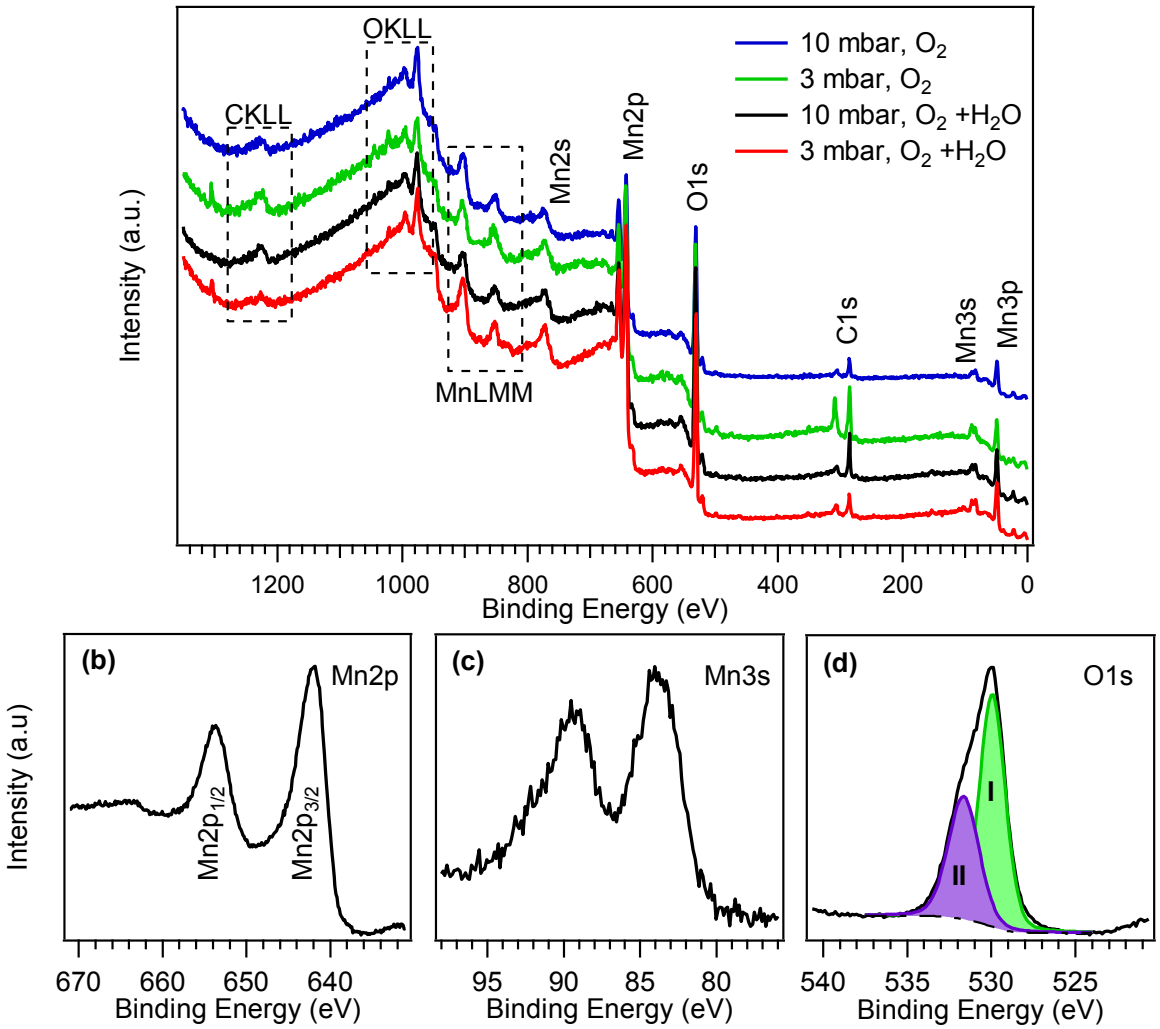

Figure 3. Surface XPS spectra: (a) wide-scans (surveys) for manganese oxide specimens. High resolution Mn2p (b), Mn3s (c) and O1s (d) photoelectron peaks for a Mn_3O_4 film deposited at 10.0 mbar under O_2+H_2O atmospheres.

The O1s signal (Figure 3d) resulted from the concomitant contribution of lattice oxygen

bonds; BE = 529.9 eV) and surface adsorbed oxygen/hydroxyl/carbonate species resulting from atmospheric exposure (BE = 531.7 eV).[11-12,28-29,34,40] As a consequence, the O/Mn atomic ratio was slightly higher than the stoichiometric one (≈ 1.7). The energy difference between the $Mn2p_{3/2}$ maximum and the lowest O1s BE component yielded a value of 111.9 eV, in line with Mn_3O_4 presence.[34]

Complementary information on the in-depth composition were gained by SIMS analysis. Irrespective of the preparation conditions, carbon content was lower than 100 ppm, indicating an appreciable system purity. As shown in Figure S4, manganese and oxygen signals had a parallel trend throughout the investigated depth, confirming the uniform composition of the target films. At a depth of ≈ 350 nm, the net decrease of Mn and O ionic yields and the concomitant increase of the Si one evidenced a relatively sharp film/substrate interface.

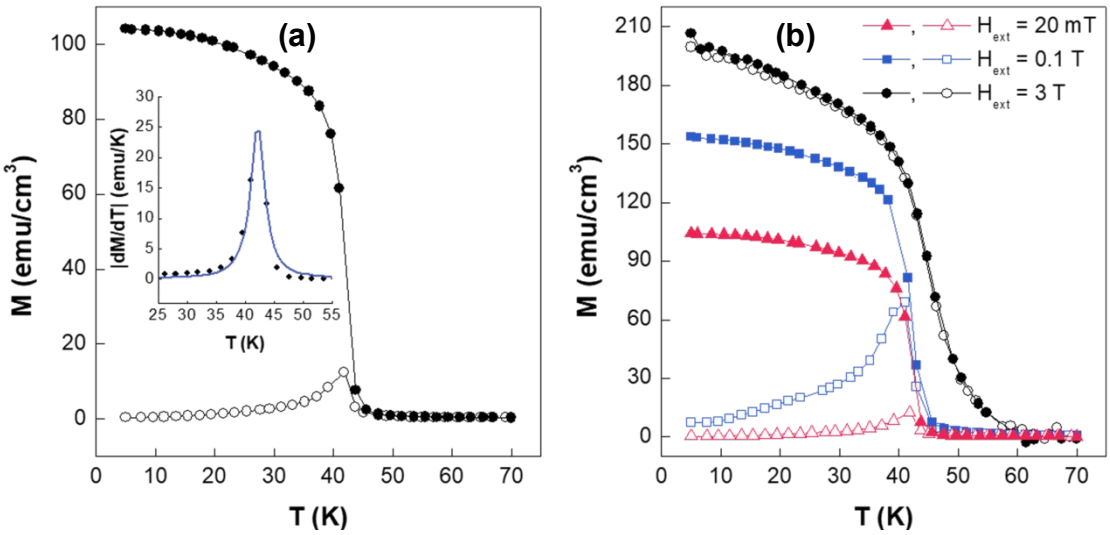

Figure 4. (a) FC (–●–) and ZFC (–○–) curves of a Mn_3O_4 sample obtained in O_2+H_2O at 3.0 mbar; inset: absolute value of the derivative |dM/dT| of the FC curve. (b) FC (filled dots) and ZFC (open dots) curves of the same specimen measured under different applied fields.

In order to investigate the interplay between the sample preparative conditions and the corresponding magnetic properties, field- and temperature-dependent magnetization measurements were performed. Figures 4a and S5 show the temperature dependence of the

field-cooled (FC) and zero-field-cooled (ZFC) magnetization measured under a magnetic field of 20 mT applied in the film plane. In the ZFC process, the film was cooled from 70 to 5 K in the absence of the magnetic field, and the magnetization was measured during the heating process under a magnetic field of 20 mT. In the FC process, a field of 20 mT was applied during cooling, and the magnetization measurement was performed upon heating under the same magnetic field.

The sharp magnetization increase observed in the FC curve corresponds to the onset of the paramagnetic-ferrimagnetic phase transition. Fitting the derivative of the FC magnetization curve (inset of Figure 4a) allowed to estimate the phase transition temperature by the position of the observed maximum. As a result, an average value of 42 K was measured for all the samples (Table 1), in excellent agreement with the transition temperature reported for α-Mn_3O_4 bulk phase.[21,33,41-42] The cusp appearing in the ZFC magnetization curve at the transition temperature could be related to the large magneto-crystalline anisotropy value of the α-Mn_3O_4 phase ($K_{mc} \approx 1.5\times10^5$ J/m^3),[41] which, in turn, leads to a high magnetic coercivity that increases at low temperatures. Under these conditions (starting from 5 K), the 20 mT applied field is not large enough to overcome the high coercivity, resulting thus in a small ZFC magnetization. Upon increasing the temperature, the magnetization rises due to the gradual reduction of the coercive field and then abruptly drops due to the loss of the long-range ferrimagnetic order when the transition temperature is approached. In order to corroborate such conclusions, FC and ZFC curves were collected under larger external fields (Figure 4b). Increasing the applied field up to 0.1 T does not affect the overall shape of the ZFC magnetization curve, and only a magnetization enhancement around the transition temperature is observed. When the applied field is increased up to 3 T, *i.e.* a value large enough to reach saturation, the cusp disappeared, confirming thus the high magnetic anisotropy of the samples and the above reported observations.

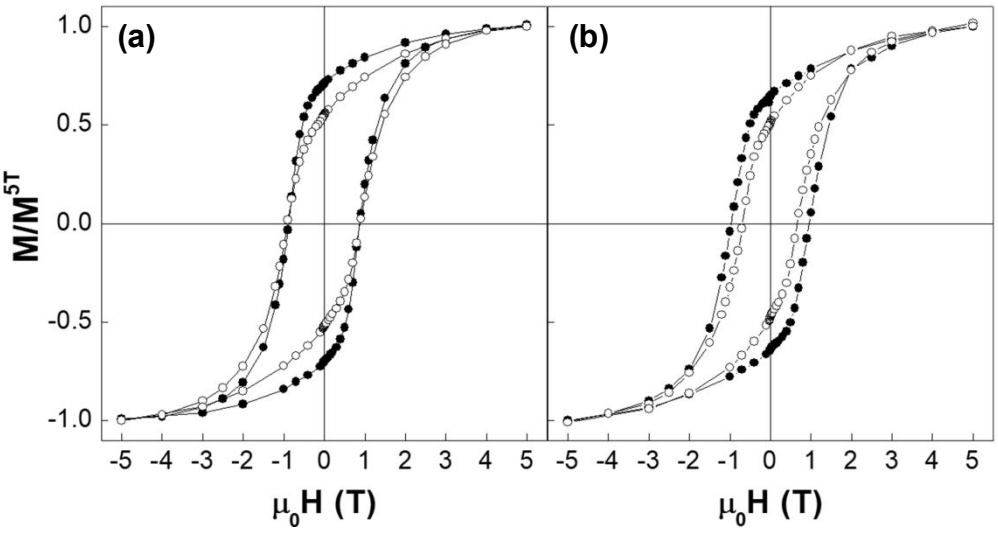

Figure 5. Low temperature (5 K) in-plane (–●–) and out-of-plane (–○–) field-dependent magnetization loops of samples Mn_3O_4 samples obtained: (a) in O_2+H_2O at 3.0 mbar; (b) in dry O_2 at 10.0 mbar. The vertical axis is normalized to the magnetization value at H = 5 T (M^{5T}).

Figures 5 and S6 display the low temperature (5 K) field-dependent magnetization loops of Mn_3O_4 films measured with the field applied either in the film plane or along the surface normal. The similarity of in-plane and out-of-plane loops suggests the lack of a well-defined magnetic anisotropy symmetry. Only a slightly preferential in-plane anisotropy is observed, as indicated by the weakly larger values of remanent magnetization and coercivity (the latter effect being observed only for samples fabricated in dry O_2) when measurements are performed within the film plane. In α-Mn_3O_4 films, the magneto-crystalline anisotropy, which forces the magnetization to lie along specific crystallographic directions (called easy-axis/plane), is expected to be the dominant contribution to the effective magnetic anisotropy. Its value is indeed almost one order of magnitude higher than the shape anisotropy (which would favor the magnetization alignment along the film plane), whose upper limit for a uniformly magnetized and infinite thin film corresponds to $1/2\mu_0 M_s^2 = 0.2\times10^5$ J/m^3, where μ_0 and M_s are the vacuum permeability and the saturation magnetization, respectively. However, the (001) plane and the <001> crystallographic direction, which represent the magneto-

crystalline easy-plane and hard-axis, respectively, are randomly distributed, thus giving rise to a similar magnetic response along different directions. The slightly preferential in-plane anisotropy could be due to the shape anisotropy of the films. The random distribution of the easy-axes can also explain the linear contribution observed in the high-field region.

Notably, all the analyzed samples showed extraordinarily large in-plane coercivity values (Table 1), significantly higher than that reported for bulk α-Mn_3O_4 at 5 K (≈ 0.3 T).[41-42] Overall, the coercivity was higher for samples obtained under dry O_2, and increased for the systems obtained at higher pressures. To the best of our knowledge, the measured coercivity values are the highest among those reported in the literature for these systems in the form of films,[20,32] and similar (or slightly lower) values have been only obtained in nanoparticles[23-24,30-31] and nanowires/rods[19-22,29,33] where surface and shape anisotropy, respectively, were indicated as the main responsible for the observed effects. In the present case, the high coercivity values could be traced back to the presence of microstructural defects (see the above discussed XRD results) acting as pinning sites for domain wall motion.[43-44] This observation accounts for the highest coercivity being observed for the Mn_3O_4 specimen synthesized under dry O_2 at 10.0 mbar, which presented the larger amount of microstructural defects, as indicated by structural analyses (see above).

■ CONCLUSIONS

In summary, high-quality Mn_3O_4 films consisting of uniformly interconnected nanoaggregates were obtained by a CVD route. Controlled variations of the growth atmosphere and working pressure enabled to tailor the preferential crystallographic orientation and film morphology, while maintaining the same phase composition, corresponding to pure tetragonal α-Mn_3O_4 (*haussmannite*) free from other manganese oxides. All the target systems showed bulk-like

magnetic properties together with an extraordinarily high low-temperature in-plane coercivity, which was traced back to the occurrence of microstructural defects. The successful fabrication of the target Mn_3O_4 materials demonstrated in this work is a key requirement for their ultimate mastering towards eventual end-uses. In fact, the present studies can trigger both fundamental and applied advancements towards the exploitation of *a*-Mn_3O_4 film properties in various tecnological applications.

■ ASSOCIATED CONTENT

Supporting Information. The Supporting Information is available free of charge on the ACS Publication website at DOI: 10.1021/acsanm.XXX-

Details and further data on XRD, FE-SEM, TEM, EELS and magnetic measurements.

Author Contributions

The manuscript was written through contributions of all authors. All authors have given approval to the final version of the manuscript.

Notes

The authors declare no competing financial interest.

Conflict of interests

The authors declare no conflict of interests.

■ ACKNOWLEDGMENTS

The authors thank Padova University DOR 2016–2018 and P-DiSC #03BIRD2016-UNIPD projects. Funding from Generalitat de Catalunya 2017 SGR 327, the Spanish MINECO

ENE2017-85087-C3-3-R and Severo Ochoa Program SEV-2017-0706, as well as CERCA Programme/Generalitat de Catalunya is also acknowledged. Part of the present work has been performed in the framework of Universitat Autònoma de Barcelona Materials Science PhD program.

■ REFERENCES

(1) Scialabba, C.; Puleio, R.; Peddis, D.; Varvaro, G.; Calandra, P.; Cassata, G.; Cicero, L.; Licciardi, M.; Giammona, G. Folate Targeted Coated SPIONs as Efficient Tool for MRI. *Nano Res.* **2017**, *10*, 3212-3227.

(2) Rizzuti, A.; Dassisti, M.; Mastrorilli, P.; Sportelli, M. C.; Cioffi, N.; Picca, R. A.; Agostinelli, E.; Varvaro, G.; Caliandro, R. Shape-Control by Microwave-Assisted Hydrothermal Method for the Synthesis of Magnetite Nanoparticles using Organic Additives. *J. Nanopart. Res.* **2015**, *17*, 408.

(3) Aslibeiki, B.; Varvaro, G.; Peddis, D.; Kameli, P. Particle Size, Spin Wave and Surface Effects on Magnetic Properties of $MgFe_2O_4$ Nanoparticles. *J. Magn. Magn. Mater.* **2017**, *422*, 7-12.

(4) Xu, J.; Sun, Y.; Lu, M.; Wang, L.; Zhang, J.; Tao, E.; Qian, J.; Liu, X. Fabrication of the Porous $MnCo_2O_4$ Nanorod Arrays on Ni Foam as an Advanced Electrode for Asymmetric Supercapacitors. *Acta Mater.* **2018**, *152*, 162-174.

(5) Ray, C.; Dutta, S.; Negishi, Y.; Pal, T. A New Stable Pd–Mn_3O_4 Nanocomposite as an Efficient Electrocatalyst for the Hydrogen Evolution Reaction. *Chem. Commun.* **2016**, *52*, 6095-6098.

(6) Bigiani, L.; Maccato, C.; Gasparotto, A.; Sada, C.; Barreca, D. Structure and Properties of Mn_3O_4 Thin Films Grown on Single Crystal Substrates by Chemical Vapor Deposition. *Mater. Chem. Phys.* **2019**, *223*, 591-596.

(7) Yang, Y.; Huang, X.; Xiang, Y.; Chen, S.; Guo, L.; Leng, S.; Shi, W. Mn_3O_4 with Different Morphologies Tuned Through One-Step Electrochemical Method for High-Performance Lithium-Ion Batteries Anode. *J. Alloys Compd.* **2019**, *771*, 335-342.

(8) Wang, Z.; Yang, D.; Sham, T.-K. Effect of Oxidation State of Manganese in Manganese Oxide Thin Films on their Capacitance Performances. *Surf. Sci.* **2018**, *676*, 71-76.

(9) Zhang, X.; Sun, X.; Chen, Y.; Zhang, D.; Ma, Y. One-Step Solvothermal Synthesis of Graphene/Mn_3O_4 Nanocomposites and their Electrochemical Properties for Supercapacitors. *Mater. Lett.* **2012**, *68*, 336-339.

(10) Xing, S.; Zhou, Z.; Ma, Z.; Wu, Y. Facile Synthesis and Electrochemical Properties of Mn_3O_4 Nanoparticles with a Large Surface Area. *Mater. Lett.* **2011**, *65*, 517-519.

(11) Zhang, H.; Liu, D.; Wei, Y.; Li, A.; Liu, B.; Yuan, Y.; Zhang, H.; Li, G.; Zhang, F. Fabrication of a 1D Mn_3O_4 Nano-Rod Electrode for Aqueous Asymmetric Supercapacitors and Capacitive Deionization. *Inorg. Chem. Front.* **2019**, DOI: 10.1039/C8QI00993G.

(12) Liu, C.; Chen, Y.; Huang, W.; Situ, Y.; Huang, H. Birnessite Manganese Oxide Nanosheets Assembled on Ni Foam as High-Performance Pseudocapacitor Electrodes: Electrochemical Oxidation Driven Porous Honeycomb Architecture Formation. *Appl. Surf. Sci.* **2018**, *458*, 10-17.

(13) Radhamani, A. V.; Ramachandra Rao, M. S. Tunable Supercapacitance of Electrospun Mn_3O_4 Beaded Chains via Charge-Discharge Cycling and Control Parameters. *Appl. Surf. Sci.* **2017**, *403*, 601-611.

(14) Wang, Z.-H.; Yuan, L.-X.; Shao, Q.-G.; Huang, F.; Huang, Y.-H. Mn_3O_4 Nanocrystals Anchored on Multi-Walled Carbon Nanotubes as High-Performance Anode Materials for Lithium-Ion Batteries. *Mater. Lett.* **2012**, *80*, 110-113.

(15) Sambandam, B.; Soundharrajan, V.; Song, J.; Kim, S.; Jo, J.; Tung, D. P.; Kim, S.; Mathew, V.; Kim, J. A sponge Network-Shaped Mn_3O_4/C Anode Derived from a

Simple, One-Pot Metal Organic Framework-Combustion Technique for Improved Lithium Ion Storage. *Inorg. Chem. Front.* **2016**, *3*, 1609-1615.

(16) Maccato, C.; Bigiani, L.; Carraro, G.; Gasparotto, A.; Sada, C.; Comini, E.; Barreca, D. Toward the Detection of Poisonous Chemicals and Warfare Agents by Functional Mn_3O_4 Nanosystems. *ACS Appl. Mater. Interfaces* **2018**, *10*, 12305-12310.

(17) Bigiani, L.; Maccato, C.; Carraro, G.; Gasparotto, A.; Sada, C.; Comini, E.; Barreca, D. Tailoring Vapor-Phase Fabrication of Mn_3O_4 Nanosystems: From Synthesis to Gas-Sensing Applications. *ACS Appl. Nano Mater.* **2018**, *1*, 2962-2970.

(18) Ma, Y.; Jiang, J.; Zhu, A.; Tan, P.; Bian, Y.; Zeng, W.; Cui, H.; Pan, J. Enhanced Visible-Light Photocatalytic Degradation by Mn_3O_4/CeO_2 Heterojunction: a Z-Scheme System Photocatalyst. *Inorg. Chem. Front.* **2018**, *5*, 2579-2586.

(19) Du, C.; Yun, J.; Dumas, R. K.; Yuan, X.; Liu, K.; Browning, N. D.; Pan, N. Three-Dimensionally Intercrossing Mn_3O_4 Nanowires. *Acta Mater.* **2008**, *56*, 3516-3522.

(20) Guo, L. W.; Peng, D. L.; Makino, H.; Inaba, K.; Ko, H. J.; Sumiyama, K.; Yao, T. Structural and Magnetic Properties of Mn_3O_4 Films Grown on MgO(001) Substrates by Plasma-Assisted MBE. *J. Magn. Magn. Mater.* **2000**, *213*, 321-325.

(21) Wang, Z. H.; Geng, D. Y.; Zhang, Y. J.; Zhang, Z. D. Morphology, Structure and Magnetic Properties of Single-Crystal Mn_3O_4 Nanorods. *J. Cryst. Growth* **2008**, *310*, 4148-4151.

(22) Tan, Y.; Meng, L.; Peng, Q.; Li, Y. One-Dimensional Single-Crystalline Mn_3O_4 Nanostructures with Tunable Length and Magnetic Properties of Mn_3O_4 Nanowires. *Chem. Commun.* **2011**, *47*, 1172-1174.

(23) Bose, V. C.; Biju, V. Defect Dependent Optical, Electrical and Magnetic Properties of Nanostructured Mn_3O_4. *Superlattices Microstruct.* **2015**, *88*, 287-298.

(24) Salazar-Alvarez, G.; Sort, J.; Suriñach, S.; Baró, M. D.; Nogués, J. Synthesis and Size-Dependent Exchange Bias in Inverted Core−Shell MnO|Mn_3O_4 Nanoparticles. *J. Am. Chem. Soc.* **2007**, *129*, 9102-9108.

(25) Muscas, G.; Singh, G.; Glomm, W. R.; Mathieu, R.; Kumar, P. A.; Concas, G.; Agostinelli, E.; Peddis, D. Tuning the Size and Shape of Oxide Nanoparticles by Controlling Oxygen Content in the Reaction Environment: Morphological Analysis by Aspect Maps. *Chem. Mater.* **2015**, *27*, 1982-1990.

(26) Peddis, D.; Cannas, C.; Musinu, A.; Ardu, A.; Orrù, F.; Fiorani, D.; Laureti, S.; Rinaldi, D.; Muscas, G.; Concas, G.; Piccaluga, G. Beyond the Effect of Particle Size: Influence of $CoFe_2O_4$ Nanoparticle Arrangements on Magnetic Properties. *Chem. Mater.* **2013**, *25*, 2005-2013.

(27) Li, L.; Liang, J.; Kang, H.; Fang, J.; Luo, M.; Jin, X. TEA-assisted Synthesis of Single-Crystalline Mn_3O_4 Octahedrons and their Magnetic Properties. *Appl. Surf. Sci.* **2012**, *261*, 717-721.

(28) Huang, H.; Yu, Q.; Peng, X.; Ye, Z. Single-Unit-Cell Thick Mn_3O_4 Nanosheets. *Chem. Commun.* **2011**, *47*, 12831-12833.

(29) Sambasivam, S.; Li, G. J.; Jeong, J. H.; Choi, B. C.; Lim, K. T.; Kim, S. S.; Song, T. K. Structural, Optical, and Magnetic Properties of Single-Crystalline Mn_3O_4 Nanowires. *J. Nanopart. Res.* **2012**, *14*, 1138.

(30) Wang, N.; Guo, L.; He, L.; Cao, X.; Chen, C.; Wang, R.; Yang, S. Facile Synthesis of Monodisperse Mn_3O_4 Tetragonal Nanoparticles and Their Large-Scale Assembly into Highly Regular Walls by a Simple Solution Route. *Small* **2007**, *3*, 606-610.

(31) Chen, B.; Rao, G.; Wang, S.; Lan, Y.; Pan, L.; Zhang, X. Facile Synthesis and Characterization of Mn_3O_4 Nanoparticles by Auto-Combustion Method. *Mater. Lett.* **2015**, *154*, 160-162.

(32) Huang, S.; Wang, Y.; Wang, Z.; Zhao, K.; Shi, X.; Lai, X.; Zhang, L. Structural, Magnetic and Magnetodielectric Properties of the Mn_3O_4 Thin Films Epitaxially Grown on $SrTiO_3$ (001) Substrates. *Solid State Commun.* **2015**, *212*, 25-29.

(33) Chang, Y. Q.; Yu, D. P.; Long, Y.; Xu, J.; Luo, X. H.; Ye, R. C. Large-Scale Fabrication of Single-Crystalline Mn_3O_4 Nanowires via Vapor Phase Growth. *J. Cryst. Growth* **2005**, *279*, 88-92.

(34) Bigiani, L.; Barreca, D.; Gasparotto, A.; Sada, C.; Martí-Sanchez, S.; Arbiol, J.; Maccato, C. Controllable Vapor Phase Fabrication of F:Mn_3O_4 Thin Films Functionalized with Ag and TiO_2. *CrystEngComm* **2018**, *20*, 3016-3024.

(35) Maccato, C.; Bigiani, L.; Carraro, G.; Gasparotto, A.; Seraglia, R.; Kim, J.; Devi, A.; Tabacchi, G.; Fois, E.; Pace, G.; Di Noto, V.; Barreca, D. Molecular Engineering of Mn^{II} Diamine Diketonate Precursors for the Vapor Deposition of Manganese Oxide Nanostructures. *Chem. Eur. J.* **2017**, *23*, 17954-17963.

(36) Tan, H.; Verbeeck, J.; Abakumov, A.; Van Tendeloo, G. Oxidation State and Chemical Shift Investigation in Transition Metal Oxides by EELS. *Ultramicroscopy* **2012**, *116*, 24-33.

(37) Briggs, D.; Seah, M. P. *Practical Surface Analysis: Auger and X-ray Photoelectron Spectroscopy*, 2nd ed.; John Wiley & Sons: New York, 1990.

(38) Li, X.; Liu, P. F.; Zhang, L.; Zu, M. Y.; Yang, Y. X.; Yang, H. G. Enhancing Alkaline Hydrogen Evolution Reaction Activity through Ni–Mn_3O_4 Nanocomposites. *Chem. Commun.* **2016**, *52*, 10566-10569.

(39) Pattern N° 024-0734, JCPDS (2000).

(40) Moulder, J. F.; Stickle, W. F.; Sobol, P. E.; Bomben, K. D. *Handbook of X-ray Photoelectron Spectroscopy*, Perkin Elmer Corporation, Eden Prairie, MN, USA 1992.

(41) Dwight, K.; Menyuk, N. Magnetic Properties of Mn_3O_4 and the Canted Spin Problem. *Phys. Rev.* **1960**, *119*, 1470-1479.

(42) Suzuki, T.; Katsufuji, T. Magnetodielectric Properties of Spin-Orbital Coupled System Mn_3O_4. *Phys. Rev. B: Condens. Matter* **2008**, *77*, 220402.

(43) Alexandrakis, V.; Wallisch, W.; Hamann, S.; Varvaro, G.; Fidler, J.; Ludwig, A. Combinatorial Development of Fe–Co–Nb Thin Film Magnetic Nanocomposites. *ACS Comb. Sci.* **2015**, *17*, 698-703.

(44) Singh, A.; Neu, V.; Fähler, S.; Nenkov, K.; Schultz, L.; Holzapfel, B. Relevance of Pinning, Nucleation, and Interaction in Nanograined Epitaxial Hard Magnetic $SmCo_5$ Films. *Phys. Rev. B: Condens. Matter* **2009**, *79*, 214401.

TOC Graphic